^{93}Nb magic angle spinning NMR study of perovskite relaxor ferroelectrics $(1-x)\mathrm{Pb}(\mathrm{Mg}_{1/3}\mathrm{Nb}_{2/3})\mathrm{O}_3-x\mathrm{Pb}(\mathrm{Sc}_{1/2}\mathrm{Nb}_{1/2})\mathrm{O}_3$

Gina L. Hoatson,[1,*] Donghua H. Zhou,[1] Franck Fayon,[2] Dominique Massiot,[2] and Robert L. Vold[3]

[1]*Department of Physics, College of William and Mary, P. O. Box 8795, Williamsburg, Virginia 23187-8795*

[2]*Centre de Recherche sur les Matériaux à Haute Température, CNRS, 1D avenue de la Recherche Scientifique, 45071 Orléans cedex 2, France*

[3]*Department of Applied Science, College of William and Mary, P. O. Box 8795, Williamsburg, Virginia 23187-8795*

^{93}Nb NMR has been used to investigate the local structure and cation order/disorder in solid solutions of $(1-x)\mathrm{Pb}(\mathrm{Mg}_{1/3}\mathrm{Nb}_{2/3})\mathrm{O}_3-x\mathrm{Pb}(\mathrm{Sc}_{1/2}\mathrm{Nb}_{1/2})\mathrm{O}_3$, as a function of concentration x. These relaxor ferroelectric solid solutions have been well characterized by x-ray diffraction, transmission electron microscopy, and dielectric response measurements. NMR magic angle spinning (MAS) spectra are presented for ^{93}Nb at 14.0 and 19.6 T. Seven narrow peaks and two broad components are observed. Narrow peaks are assigned to configurations of ^{93}Nb nuclei with only Mg^{2+} and/or Sc^{3+} (no Nb^{5+}) cations occupying the six nearest B neighbor sites (nBn); and are designated 0–6 according to the number of Mg^{2+} cations in the nBn configuration. The two broad components are assigned to configurations with more than one Nb^{5+} cation in the nearest B sites. In order to fit the MAS line shapes it is necessary to include distributions of the electric-field gradient parameters and dispersions in isotropic chemical shifts; these have been obtained from the data. The relative intensities of each spectral component are analyzed and the data strongly support a modified random site model of B-site order. Monte Carlo simulations of B cation ordering are presented to explain the observed NMR intensities and to validate the model.

I. INTRODUCTION

The large piezoelectric and electromechanical responses of lead based perovskite relaxor ferroelectrics have resulted in their use in a variety of important technical applications: capacitors, sensors, actuators, and transducers.[1–4] These relaxor ferroelectrics show a characteristic diffuse, frequency-dependent para- to ferroelectric phase transition.[1] The microscopic origin of this relaxor behavior is still not well understood. For lead based $AB\mathrm{O}_3$ perovskites to exhibit relaxor behavior, at least one of the A- or B-sites should have variable composition. The complex B-site solid solutions have been studied most extensively.[1,5–7] Detailed fundamental understanding of the role of B-site order/disorder is crucial for design and fabrication of the next generation of technologically useful ferroelectric materials.

Initially in $\mathrm{Pb}(\mathrm{Mg}_{1/3}\mathrm{Nb}_{2/3})\mathrm{O}_3$ (PMN), the Mg^{2+} and Nb^{5+} ions were considered to be distributed completely randomly (CR model) on the B lattice.[8,9] However, selected-area electron diffraction and high-resolution electron microscopy (HREM) studies of PMN reveal NaCl-type nanodomains (2–5 nm) dispersed in a disordered matrix.[5–7] These nanodomains consist of alternating planes of β' and β'' sites along the [111] direction. The nonstoichiometric 1:1 ordering is believed to be the result of interplay between long-range Coulomb interactions and short-range interactions related to the covalency of the Pb-O bonds.[10] These effects have been investigated using several computational models.[11–14] The β'' sites are assumed to be exclusively occupied by Nb^{5+}; unfortunately, there is no direct experimental information on the composition of the β' sites. This leads to several competing B-site ordering models which differ in the β' site

composition.[7] For example in PMN, in the space charge model (SC), the ferroelectrically "inactive" Mg^{2+}, and ferroelectrically "active" Nb^{5+} layers are interleaved.[7] While in the random site model (RS), pure Nb^{5+} layers and mixed layers (of randomly distributed Mg^{2+} and the remaining Nb^{5+}) are interleaved.[7] In the SC model, charges are unbalanced, this should inhibit the growth of large ordered domains. Indeed for PMN, extended thermal treatment does not result in any increase in the domain size or degree of ordering. This absence of increase has been used to support the SC model.[7] However, in solid solutions of $\mathrm{Pb}(\mathrm{Mg}_{1/3}\mathrm{Ta}_{2/3})\mathrm{O}_3$ (PMT) and 5–25 mol% PbZrO_3 (PZ), Akbas *et al.* report that extended thermal treatment at elevated temperature causes the domain size and degree of ordering to increase substantially (from 20% volume in small ordered domains of 2–3 nm, to 95% volume in large domains of size about 100 nm).[15] Such pronounced domain coarsening contradicts the SC model and supports the random site model, where charge neutrality is maintained regardless of domain size. Akbas *et al.* further suggest that in PMN, the absence of increase in domain size is the result of the order-disorder transition temperature being too low for kinetic activity.[16,17]

The aim of this study is to investigate the B-site order/disorder quantitatively and thus obtain a more accurate description of local cation order. Solid state NMR is an excellent tool for this purpose, however, if NMR is to provide meaningful insights into B-site order it is essential to use carefully prepared samples whose bulk properties have been well characterized by standard methods. This paper describes a systematic investigation of solid solutions of PMN and $\mathrm{Pb}(\mathrm{Sc}_{1/2}\mathrm{Nb}_{1/2})\mathrm{O}_3$ [$(1-x)$PMN-xPSN]. The PMN-PSN ceramics were synthesized by Davies *et al.* who characterized them using x-ray diffraction (XRD), transmission electron

microscopy (TEM), and frequency-dependent dielectric measurements.[16] Measurements were performed on two sets of materials: "disordered," which were simply the as-sintered samples, and "ordered," which were obtained through prolonged annealing (24 h, 1250 °C) followed by a slow cooling (10 °C/h to 900 °C). In the TEM, the disordered samples show very limited cation order; small domains (2–3 nm) for all concentrations x. For $x > 0.1$, slow, high-temperature annealing promotes the degree of order and increases domain size; the largest ordered domains (200 nm) are observed at $x \sim 0.5$. The increased compositional order is attributed to the size, charge, and electronegativity differences of the Nb^{5+} and Mg^{2+}/Sc^{3+} ions. Dielectric results indicate that relaxor ferroelectric behavior is observed for all compositions in the disordered samples and for $x < 0.5$ in well-ordered samples. Ordered samples with high scandium concentrations exhibit normal ferroelectric behavior, with the crossover from relaxor to normal ferroelectric behavior occurring at concentrations $0.5 < x < 0.6$.

There are only a few NMR studies of PMN based relaxor ferroelectrics.[18–21] Glinchuk *et al.* have studied the PMN-PSN system using stationary samples at low magnetic fields (5.7 and 7 T) where the low spectral resolution precludes definitive conclusions on B-site ordering.[18] Cruz *et al.* have performed magic-angle spinning (MAS) and three-quantum MAS (3QMAS) ^{93}Nb NMR on PMN at 9.4-T field.[19] Shore and co-workers present nutation experiments on PMN, and nutation (at 9.4 T) and MAS (at 14 T) on PMN-PT (PbTiO$_3$) solid solutions.[20,21] All ^{93}Nb MAS spectra reported for PMN-PT have one narrow and one broad line. The broad peak is believed to arise from at least two overlapping line shapes. Shore *et al.* associate these three components with cubic, axial, and rhombic symmetry of nearest B-site neighbor environments, respectively.[21]

In solid-state NMR, high speed magic-angle spinning removes broadening arising from second rank tensor interactions, including the chemical shift, dipolar, and first-order quadrupolar anisotropies; it also reduces broadenings due to fourth rank tensor interactions, including second-order quadrupolar, and second-order dipolar interactions.[22] In ^{93}Nb MAS experiments on PMN-PSN, the dominant interactions are the isotropic chemical shift and second-order quadrupolar coupling. When expressed in ppm, the former (δ_{iso}^{CS}) is independent of magnetic field, while both the isotropic shift (δ_{iso}^{2Q}) and linewidth (Δ^{2Q}) of the latter are inversely proportional to the square of the magnetic field. This means that higher magnetic fields result in better spectral resolution. In an attempt to optimize the spectral resolution, experiments have been performed at high magnetic fields (14 and 19.6 T) using MAS probes capable of fast spinning ($\nu_R = 30$–35 kHz). For the PMN-PSN solid solutions, seven narrow lines and two broad features are resolved; more lines are observed than for PMN-PT system.[21] This allows the assignment of specific nearest B neighbor configurations and quantitative comparison of experimental results with predictions of competing B-site ordering models.

Following the experimental details in Sec. II, the MAS spectra are presented and analyzed in the result section (Sec. III). Spectral components are assigned to nearest B cation

neighbor configurations in Sec. IV. The assignment allows the prediction of MAS spectra by several B-site ordering models, these are compared with experimental results in Sec. V. The implications of the results for cation ordering and the consistency of PMN NMR parameters with existing literature are discussed in Sec. VI. Finally Sec. VII contains the conclusions on B cation disorder in these relaxor ferroelectric solid solutions.

II. EXPERIMENT

The $(1-x)$PMN-xPSN ceramics were were available in the following concentration; $x = 0$, 0.2, 0.6, 0.7, 0.9 for disordered samples and $x = 0.1$, 0.2, 0.6, 0.7, 0.9 for ordered samples.[16]

Single pulse ^{93}Nb MAS spectra were collected at three magnetic fields, 9.4, 14, and 19.6 T (proton frequencies of 400, 600, and 833 MHz, respectively). Spectral resolution at 9.4 T was not satisfactory and only MAS spectra collected at 14 and 19.6 T were analyzed in detail. For the experiments at 9.4 T, the ^{93}Nb Larmor frequency $\nu_L = 97.95$ MHz, rotor diameter was 4 mm, sample spinning speed $\nu_R = 12$ kHz, rf field strength $\nu_1 = 50$ kHz, pulse duration $t_p = 1$ μs, and relaxation delay $d = 50$ ms. For experiments at 14 T, $\nu_L = 146.9$ MHz, rotor diameter was 2.5 mm, $\nu_R = 34$ kHz, $\nu_1 = 50$ kHz, $t_p = 1$ μs, and $d = 200$ ms. For experiments at 19.6 T, $\nu_L = 203.0$ MHz, rotor diameter was 2 mm, $\nu_R = 35$ kHz, $\nu_1 = 71$ kHz, $t_p = 0.7$ μs, and $d = 100$ ms. Typically the number of scans acquired was 3000, the full spectral width was 1 MHz (dwell time 1 μs), 4096 complex data points were collected, and NbCl$_5$ in acetonitrile was used as the chemical shift reference ($\delta_{iso}^{CS} = 0$ ppm).

Spectra collected at 14 T were processed using Bruker XWIN software, with 100 Hz exponential multiplication, Fourier transformation, and phase correction of both zeroth and first order. Spectra collected at 19.6 T were processed using NMRPIPE,[23] with three points left shift, ten points backward linear prediction, followed by 100-Hz exponential multiplication, Fourier transformation, and zeroth order phase correction. Both sets of spectra were then imported into DMFIT,[24] base line corrected using cubic splines method, and the central transition ($+1/2 \leftrightarrow -1/2$) was systematically deconvoluted into component lines.

III. RESULTS

At both 14 and 19.6 T, the central transition of the ^{93}Nb MAS spectra of PMN consists of one sharp and one broad peak (Fig. 1), in agreement with the literature.[19,21] Field-dependent shifts are observed for both peaks and the linewidth of the broad peak is substantially narrower at the higher field. These two phenomena result from the inverse square dependence on field strength of both the second-order quadrupolar isotropic shift (δ_{iso}^{2Q}) and the second-order quadrupolar linewidth (Δ^{2Q}). ^{93}Nb is a quadrupolar nucleus with spin $I = 9/2$, and therefore interacts with the local electric-field gradient (EFG), as well as the internal and external magnetic fields. Under magic-angle spinning, the central transition ($+1/2 \leftrightarrow -1/2$) frequency is influenced by
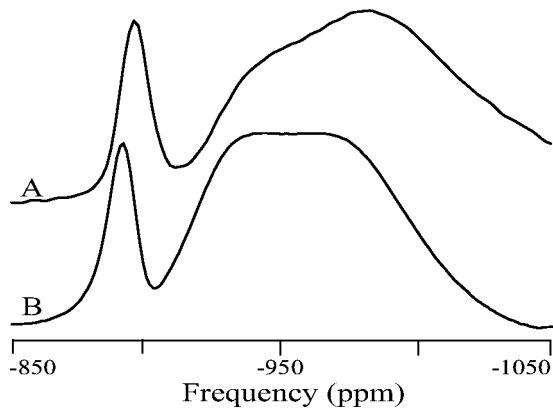
FIG. 1. ^{93}Nb MAS spectra of PMN collected at 14 T, with magic angle spinning speed $\nu_R = 34$ kHz (A), and at 19.6 T with $\nu_R = 35$ kHz (B).

FIG. 2. The seven narrow peaks in ^{93}Nb MAS spectra for $(1-x)$PMN-xPSN separated by 14 ppm approximately. Spectra are collected at at 19.6 T, with sample spinning speed 35 kHz. From top to bottom, concentrations $x = 0$, 0.2, 0.7, and 0.9. The last three samples are ordered materials.

three terms: isotropic chemical shift δ_{iso}^{CS}, isotropic second-order quadrupolar shift δ_{iso}^{2Q}, and anisotropic second-order quadrupolar broadening, respectively.[25] When expressed in ppm, the observed central $(+1/2 \leftrightarrow -1/2)$ transition frequency is

$$\delta_{1/2} = \delta_{iso}^{CS} - A P_Q^2 + A P_Q^2 F(\theta, \phi, \eta), \qquad (1)$$

where (θ, ϕ) define the crystallite orientation, F is an orientation dependent function which averages to zero and is responsible for the powder pattern line shape, the factor is

$$A \equiv \frac{3 \times 10^5 [I(I+1) - 3/4]}{[2I(2I-1)]^2 \nu_L^2},$$

and the quadrupolar product is $P_Q \equiv C_Q \sqrt{1 + \eta^2/3}$. The quadrupolar coupling constant is defined as $C_Q = e^2 q_{zz} Q/h$, where h is the Planck's constant, e is the electron charge (magnitude), q_{zz} is the principle component of the EFG tensor, and η is the EFG asymmetry parameter. The ''position,'' or the ''mass center'' of the line shape is determined by $\langle \delta_{1/2} \rangle = \delta_{iso}^{CS} - A P_Q^2$, where $\langle \; \rangle$ means averaging over all orientations. Both parts of the second-order quadrupolar interaction are inversely proportional to the square of the Larmor frequency, and thus magnetic-field strength (or if expressed in Hz, inversely proportional to the field). Thus from the field-dependent shift, P_Q may be estimated. For example, between 14 and 19.6 T the observed 5-ppm shift of the sharp peak in PMN spectra yields an crude estimate of the quadrupole product $P_Q = 13$ MHz.

At both field strengths, manifolds of spinning side bands are observed in the MAS spectra (not shown) because of first-order quadrupolar contributions of satellite transitions (ST's). Each sideband has similar line shape as that of the central transition $(1/2 \leftrightarrow -1/2)$; one narrow and one broad peak. The sidebands arise mainly from the $\pm 3/2 \leftrightarrow \pm 1/2$ transitions. No separate sidebands due to outer transitions are observed. This could be either because of their low intensities or the broad line shapes, which cause the overlapping of different sets of sidebands. The span of the side band mani-
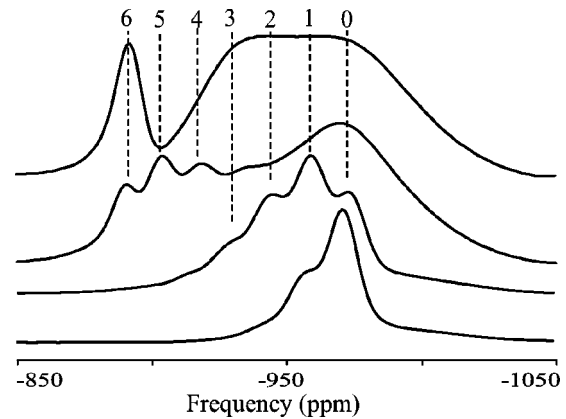
fold is approximately $2\nu_Q$, which is the width of the powder pattern for the first satellite transitions of half integral $(I > 1)$ spins,[26] with definition

$$\nu_Q \equiv \frac{3C_Q}{2I(2I-1)}. \qquad (2)$$

The ST sidebands of the broad peak extend well beyond the 1-MHz spectral width at both fields, indicating a very large C_Q. At 19.6 T the ST sideband manifold of the narrow peak also persists over the entire 1-MHz spectral window, giving an estimated $C_Q \geq 12$ MHz. This agrees well with the value $P_Q = 13$ MHz derived from the field-dependent shift. At 14 T the manifold of the sharp peak covers only about 700 kHz, giving an estimated $C_Q \geq 8.4$ MHz. However, the higher field estimate, $C_Q \geq 12$ MHz, is probably more accurate since the narrower spectral coverage at 14 T could be influenced either by any slight misset in the magic angle or by a higher probe Q factor.

Varying the magnetic field from 14 to 19.6 T causes the MAS line shape of the broad peak to change appreciably; the former has a slanted top, while the latter is more square. This suggests that the broad peak has at least two components. The overall line shape of the broad peak can only be reproduced if distributions of both chemical shift and quadrupolar parameters are used. Presumably these result from random local environments. At the present resolution, it is only possible to distinguish two broad components, one at lower frequency (D_1) and the other at higher frequency (D_2).

The central transitions of ^{93}Nb MAS spectra are shown in Fig. 2 for several PSN concentrations. Careful comparison of the spectra at all concentrations at both fields reveals seven narrow peaks in addition to the two distributions. The positions of these narrow peaks change very little with concentration, and their positions are separated by about 14 ppm. They are labeled from low to high frequencies as 0–6 (assignments are presented in Sec. IV).

The program DMFIT (Ref. 24) was used to deconvolute the central transition MAS line shapes. The seven narrow peaks

TABLE I. Deconvolution parameters of MAS spectra for $(1-x)$PMN-xPSN solid solutions.

		Disordered, 14 T					Disordered, 19.6 T					Ordered, 19.6 T				
	x	0	0.2	0.6	0.7	0.9	0	0.2	0.6	0.7	0.9	0.1	0.2	0.6	0.7	0.9
0 [a]	center (ppm)			−983.3	−982.2	−978.8			−975.1	−975.1	−971.4			−975.4	−974.2	−971.5
	FWHM (ppm)			14.0	18.1	22.0			16.0	13.0	16.0			13.0	13.0	13.0
	I (%)			6.3	12.8	37.4			6.3	6.4	27.7			8.4	16.9	52.5
1	center (ppm)			−968.5	−966.8	−964.5			−960.3	−960.2	−957.0			−960.6	−959.2	−956.7
	FWHM (ppm)			17.6	21.3	20.0			16.0	17.9	16.0			14.3	14.3	14.3
	I (%)			19.4	29.7	10.9			17.5	23.7	15.0			21.7	31.5	25.4
2	center (ppm)			−952.2	−950.8	−948.5			−945.1	−944.3	−942.0			−945.1	−943.6	−941.7
	FWHM (ppm)			19.9	18.9	18.0			17.8	18.6	16.0			15.7	15.7	15.7
	I (%)			25.9	19.7	3.3			23.2	22.4	7.0			24.8	23.6	5.0
3	center (ppm)			−936.5	−936.0				−930.0	−928.9				−929.6	−928.9	
	FWHM (ppm)			17.4	20.4				19.3	17.0				17.0	17.0	
	I (%)			13.2	10.3				19.1	9.2				18.2	10.9	
4	center (ppm)		−924.1	−921.9	−921.3			−918.0	−915.0	−915.0			−919.0	−917.5	−915.1	−914.1
	FWHM (ppm)		14.4	15.6	15.0			15.7	15.7	15.7			15.3	15.3	15.3	15.3
	I (%)		5.4	5.4	2.5			6.3	6.4	2.7			2.4	7.0	7.0	2.9
5	center (ppm)		−911.0	−908.0	−908.0			−904.2	−902.0	−902.0			−904.9	−903.5	−901.2	−901.2
	FWHM (ppm)		14.9	16.0	17.8			15.2	15.2	14.3			13.7	13.7	13.7	13.7
	I (%)		10.3	1.4	1.2			10.6	2.9	0.5			8.5	11.3	2.7	0.7
6	center (ppm)	−895.5	−896.3				−891.0	−890.0	−887.0			−890.6	−890.0	−887.4	−887.4	
	FWHM (ppm)	12.0	17.0				12.0	15.5	15.5			12.0	12.0	12.0	12.0	
	I (%)	13.0	9.0				14.8	7.3	1.4			11.7	7.7	1.2	0.3	
D_1 [b]	I (%)	48.4	39.8	28.4	23.9	48.4	39.9	42.8	23.2	35.1	50.3	44.8	45.4	16.0	13.1	17.2
D_2 [c]	I (%)	38.6	35.6				45.3	33.0				32.6	28.6			

[a] Narrow components 0–6 are simple superpositons of 50% Gaussian and 50% Lorentzian. Error limits for both peak centers and FWHM (full width at half maximum) are estimated to be ±0.5 ppm.

[b] D_1 is the first broad component with Gaussian distributions of both $\delta_{\mathrm{iso}}^{\mathrm{CS}}$ and ν_Q. The mean $\mu(\delta_{\mathrm{iso}}^{\mathrm{CS}})$ is allowed to vary between −953 and −951 ppm, standard deviation $\sigma(\delta_{\mathrm{iso}}^{\mathrm{CS}})=10.9$ ppm, $\mu(\nu_Q)=1190$ kHz, $\sigma(\nu_Q)=163$ kHz, and the asymmetry parameter is fixed at $\eta=0.4$.

[c] D_2 is the second broad component with distributions. $\mu(\delta_{\mathrm{iso}}^{\mathrm{CS}})$ is from −922 to −919.5 ppm, $\sigma(\delta_{\mathrm{iso}}^{\mathrm{CS}})=12.9$ ppm, $\mu(\nu_Q)=1015$ kHz, $\sigma(\nu_Q)=214$ kHz, and the asymmetry parameter is fixed at $\eta=0$.

were simulated by simple line shapes; 50% Gaussian and 50% Lorentzian. Depending on the concentration of the sample, one (D_1, high x) or two broad lines (D_1 and D_2, low x) were necessary to represent the intensities that are not reproduced by the Gaussian/Lorentzian lines. In the deconvolution, these broad lines include Gaussian distributions of both isotropic chemical shifts and quadrupolar coupling constants (see Table I).

The deconvolutions of PMN MAS spectra at both 14 and 19.6 T are shown in Fig. 3. Considerable care has been taken to obtain consistent parameters at both magnetic fields. The distribution D_1 has mean $\mu(\delta_{\mathrm{iso}}^{\mathrm{CS}})=-953$ ppm, standard deviation $\sigma(\delta_{\mathrm{iso}}^{\mathrm{CS}})=10.9$ ppm, $\mu(\nu_Q)=1190$ kHz, $\sigma(\nu_Q)$ $=163$ kHz, and its asymmetry parameter is set to $\eta=0.4$ which gives good fits for both spectra. D_2 has $\mu(\delta_{\mathrm{iso}}^{\mathrm{CS}})$ $=-919.5$ ppm, $\sigma(\delta_{\mathrm{iso}}^{\mathrm{CS}})=12.9$ ppm, $\mu(\nu_Q)=1015$ kHz, $\sigma(\nu_Q)=214$ kHz, and $\eta=0$.

For PMN-PSN solid solutions, deconvolutions were performed on three sets of MAS spectra: disordered samples at 14 T, disordered samples at 19.6 T, and ordered samples at 19.6 T. The parameters for broad components are very similar to those derived for PMN; very small adjustment of the mean values of the isotropic chemical shift, $\mu(\delta_{\mathrm{iso}}^{\mathrm{CS}})$, is allowed, which varies from −953 to −951 ppm for D_1, and from −922 to −919.5 ppm for D_2. Examples of the deconvolutions are shown in Fig. 4 for concentrations $x=0.2$ and
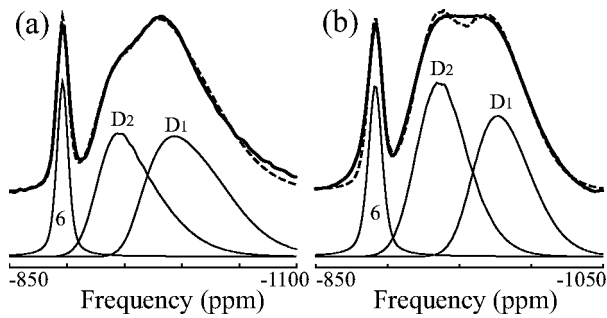
FIG. 3. Constrained deconvolution of PMN MAS spectra at 14 T (a) and 19.6 T (b). Bold solid lines are the experimental MAS spectrum, the thin solid lines are deconvoluted components 6, D_1, and D_2, and the dashed line is the sum of all components (see fitting parameters in Table I).

0.7. Very good fits are achieved for all spectra with deviation being greatest for the spectrum of the $x=0.2$ disordered sample at 14 T [Fig. 4(a)]. It is necessary to use both broad components D_1 and D_2 for low PSN concentrations ($x=0$, 0.1, and 0.2), but only D_1 is needed for high concentrations ($x=0.6$, 0.7, and 0.9). The quantitative results of the constrained deconvolution are summarized in Table I. We defer detailed discussion of the NMR parameters and the deconvolution results to Sec. VI.
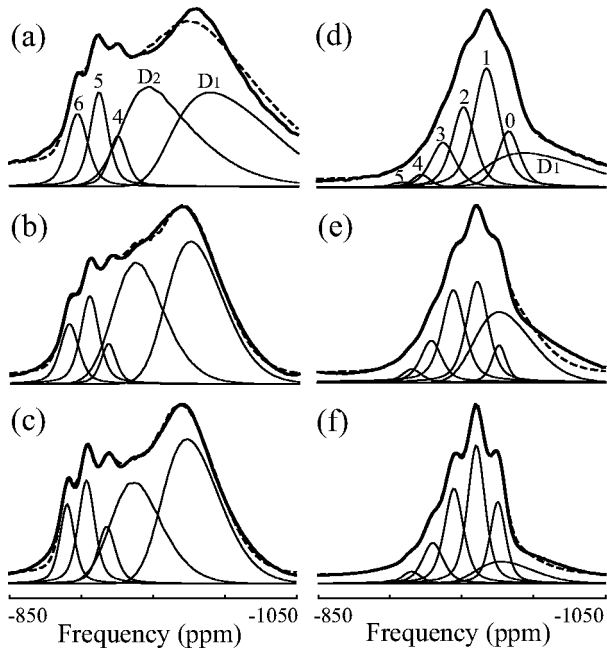

FIG. 4. Deconvolution of MAS spectra for $(1-x)$PMN-xPSN solid solutions. (a) $x=0.2$ disordered sample at 14 T. (b) $x=0.2$ disordered sample at 19.6 T. (c) $x=0.2$ ordered sample at 19.6 T. (d) $x=0.7$ disordered sample at 14 T. (e) $x=0.7$ disordered sample at 19.6 T. (f) $x=0.7$ ordered sample at 19.6 T. In each of (a)–(f), the bold solid line is the experimental spectrum, the thin solid lines are decomposed components 0–6, D_1, and D_2, and the dashed line is the sum of all components. The dashed line in several graphs is barely visible because of the good fit. Parameters are given in Table I.
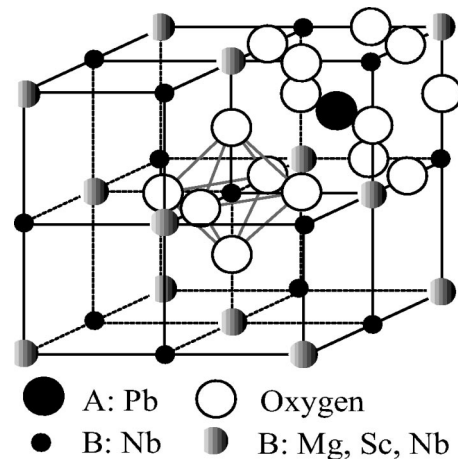

FIG. 5. Perovskite structure and B lattice for PMN-PSN. Only one complete perovskite cube and one BO_6 octahedron are displayed, so as to highlight the B-site lattice. Random B-site ordering in the [111] direction consists of alternating pure (Nb) and mixed (Mg, Sc, and Nb at random) planes.

IV. ASSIGNMENTS

We assign components of ^{93}Nb MAS spectra according to the nearest B-site neighbor (nBn) configurations. This provides a very detailed description of local cation ordering in relaxor ferroelectrics. The solid solutions PMN-PSN have perovskite structure ABO_3 (Fig. 5), with A on the cube center, B on the eight corners, and O^{2-} in the middle of the edges. Pb^{2+} cations sit on A sites, while B sites are occupied by three types of cations, Mg^{2+}, Sc^{3+}, and Nb^{5+}. For a central Nb^{5+} B cation, the nearest neighbors are six oxygen ions (octahedral), next-nearest neighbors are eight Pb^{2+} (hexahedral), and the next-next-nearest neighbors are six other B cations (octahedral) that we call nearest B neighbors (nBn). The first two shells are the same for each central B cation. However, the composition of the third shell varies ($B=Mg^{2+}$, Sc^{3+}, and Nb^{5+}). The valence charge, size, and electronegativity are different for these B cations: Mg^{2+} (ionic radius 0.72 Å, Pauling scale electronegativity 1.31), Sc^{3+} (0.745 Å, 1.36), and Nb^{5+} (0.64 Å, 1.60).[27,28] The B_6 cations interact with the central Nb^{5+} cation by electrostatic interactions, and can also modify the orientation, size, and shape of O_6 octahedra and Pb_8 hexahedra by electrostatic, covalent and steric effects. Coulombic repulsion and bond covalencies with O^{2-} tend to cooperate the displacements of Pb^{2+} and the B cations; on the other hand, the steric effect tends to break the cooperation between Pb^{2+} and smaller B cations (Nb^{5+}), by inducing Pb^{2+} to move toward the larger B cations (Mg^{2+} and Sc^{3+}).[29] It is also reported that, in several lead based perovskite relaxor ferroelectrics, size mismatch of B cations combined with the strong Pb^{2+} off-centering (up to 0.2 Å against B_6 octahedra and up to 0.5 Å against O_{12} icosahedra) causes O_6 octahedra to rotate or tilt by as much as 18°.[30] As a result, the precise configuration and ordering of the three types of cations strongly affect the electron density and electric-field gradient at the location of the central ^{93}Nb nuclei. These are manifested in the NMR chemical shift and quadrupolar coupling parameters. Thus it
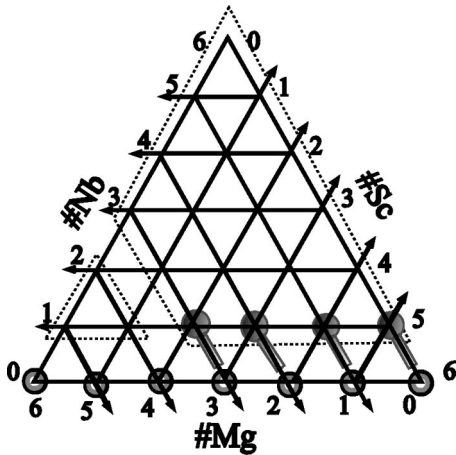
FIG. 6. The 28 nBn configurations of Nb^{5+} cations and their assignments. For a given grid point, the three vectors pointing to the axes indicate the numbers of each cation, and thus the triplet coordinate (N_{Mg}, N_{Sc}, N_{Nb}). The 18 configurations in the dotted trapezoid are assigned to broad distribution component D_1. The three configurations in the dotted triangle are assigned to broad distribution component D_2. The seven configurations on the bottom line are assigned to the narrow resonance lines. Only for concentrations $x=0.6$ and 0.7 do the four narrow lines (0,6,0), (1,5,0), (2,4,0), and (3,3,0) also include contributions from (0,5,1), (1,4,1), (2,3,1), and (3,2,1), respectively.

is reasonable to assign ^{93}Nb MAS spectral components according to the nBn configurations. The feasibility of this interpretation is strengthened by the fact that it gives consistent and sensible results for the concentration dependence of the relative integrated peak intensities.

Nearest B neighbor configurations will be designated by the numbers of Mg, Sc, and Nb cations, (N_{Mg}, N_{Sc}, N_{Nb}); each number can range from 0 to 6 with the requirement that their sum is 6. In Fig. 6, each of the 28 nBn configurations is represented by a point on a triangular grid. For a given grid point, the three vectors pointing to the axes indicate the numbers of each type of cation, and thus the triplet coordinate (N_{Mg}, N_{Sc}, N_{Nb}).

We assign the seven narrow components of the spectra (lines 6–0, see Fig. 2) to the seven nBn configurations consisting of no Nb^{5+}. They are designated by $(N_{Mg}, 6 - N_{Mg}, 0)$, with $N_{Mg} = 6, 5, \cdots 0$ and represented by the seven grid points on the bottom of the triangle in Fig. 6. Only for the concentrations $x=0.6$, 0.7 are there minor deviations; for good quantitative agreement with the intensities of the four narrow lines 3, 2, 1 and 0, the probabilities (predicted by random site model, see Sec. V) of configurations (3,2,1), (2,3,1), (1,4,1), and (0,5,1) are added to those of (3,3,0), (2,4,0), (1,5,0), and (0,6,0), respectively. The assignments are reasonable given that in strong contrast with Nb^{5+} cations, Mg^{2+} and Sc^{3+} cations have similar size and electronegativity. The nBn configurations with only Mg^{2+} and/or Sc^{3+} cation have closest to cubic symmetry, and thus small EFG's; consistent with the observed narrow linewidths.

On the other hand, size and electronegativity mismatch resulting from substituting Nb^{5+} for Mg^{2+}/Sc^{3+} severely distorts the cubic symmetry, leading to larger EFG's, conse-
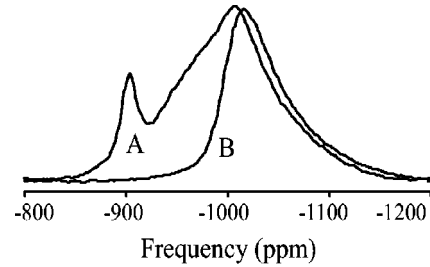

FIG. 7. Comparison of MAS spectra of PMN (A) and Pyrochlore (B). Spectra were acquired at 9.4 T with sample spinning speed 32 kHz. Figure is modified from the work of Cruz *et al.* (Ref. 19). The chemical shift was referred to Nb_2O_5 originally; and has been recalibrated to make $NbCl_5/MeCN$ as zero ppm reference. (In our PMN spectrum at 9.4 T and spinning speed 12 kHz, the sharp peak occurs at -907 ppm.)

quently greater linewidths. These broad lines, which are associated with nBn configurations containing Nb^{5+}, cannot be resolved and they contribute to the two broad distributions D_1 and D_2. The three grid points (5,0,1), (4,1,1), and (4,0,2) in the dotted triangle are assigned to the second broad component D_2 (Fig. 6). The remaining 18 grid points in the dotted trapezoid contribute to the broad distribution component D_1 (Fig. 6). Similar to the case of the narrow lines, small adjustment is made for D_1 at concentrations $x=0.6$, 0.7; D_1 now consists of only 14 nBn configurations, excluding the four configurations on the bottom line of the trapezoid.

In agreement with Fitzgerald *et al.*[21] the all-magnesium nBn configuration (6,0,0) corresponds to the high-frequency narrow peak 6 (around -900 ppm). Moreover, the all-niobium nBn configuration (0,0,6) contributes to the low-frequency broad peak D_1 (centered around -980 ppm at 14 T, and -1020 ppm at 9.4 T). The all-scandium configuration (0,6,0) is assigned to the low-frequency narrow peak 0 (around -980 ppm). These assignments are based on our experimental results and data from studies of two niobates.[19,31] First, the all-magnesium configuration can be identified by comparing the MAS spectrum of PMN (Mg:Nb $= 1:2$) to that of pyrochlore ($Pb_{1.83}[Mg_{0.29}Nb_{1.71}]O_{6.39}$, Mg:Nb$\sim1:6$), see Fig. 7.[19] In both crystalline materials, each Nb^{5+} is surrounded by six Mg^{2+} and/or Nb^{5+} cations; one notable difference, however, is that the pyrochlore has substantially lower Mg^{2+} content. Thus the population of the all-magnesium configuration (6,0,0) is predicted to be much lower in pyrochlore than that in PMN. It is obvious from Fig. 7 that the narrow peak of PMN around -907 ppm must be attributed to the all-magnesium configuration (6,0,0), since no corresponding peak is present for pyrochlore. Second, the above analysis also leads to the conclusion that in pyrochlore the broad peak (around -1020 ppm) consists of ^{93}Nb species with Nb^{5+} as the majority in their nBn configurations; (0,0,6), (1,0,5), and (2,0,4). This hypothesis is further supported by the fact that four lead niobates ($Pb_2Nb_2O_7$, $Pb_3Nb_4O_{13}$, $Pb_5Nb_4O_{15}$, and $Pb_3Nb_2O_8$) consisting of corner sharing NbO_6 octahedra have δ_{iso}^{CS} ranging from -1003 to -951 ppm and P_Q ranging from 13.6 to 20.6 MHz (or δ_{iso}^{2Q} from -27 to -62 ppm at 9.4 T).[31] This confirms that the ^{93}Nb species surrounded by six Nb^{5+} cations resonate on

the low-frequency side (from -978 to -1065 ppm at 9.4 T). Third, the lowest frequency narrow peak 0 is assigned to the all-scandium configuration (0,6,0). This is supported by the concentration dependence; the intensity of this peak increases monotonically with x. The largest intensity is observed in the $x=0.9$ spectrum (0.1 PMN– 0.9 PSN), where the concentration of scandium is largest (Fig. 2).

V. MODELS OF CATION DISORDER

We have assigned the components of MAS NMR spectra to the nearest B neighbor cation configurations, and established a relation between the integrated spectral intensities and the population of Nb^{5+} species with particular nBn configurations. Thus the experimental NMR results can be used to differentiate between various theoretical models of B-site order/disorder in perovskite ferroelectric solid solutions. The B-site ordering models can be used to predict the NMR spectral intensities, which can be directly compared to the NMR observations for all compositions x. The two most relevant models are considered in detail: the completely random (CR) model[8] and the random site (RS) model.[16]

A. Completely random model

In this simple model all B sites are assumed to be randomly occupied by Mg^{2+}, Sc^{3+}, and Nb^{5+}, and the stoichiometry depends on the concentration x; $Pb[Mg_{(1-x)/3}Sc_{x/2}Nb_{(4-x)/6}]O_3$. Assume that the three types of B cations have partial concentrations C_{Mg}, C_{Sc}, and C_{Nb} such that $C_{Mg}+C_{Sc}+C_{Nb}=1$. Thus the partial concentrations are $C_{Mg}=(1-x)/3$, $C_{Sc}=x/2$, and $C_{Nb}=(4-x)/6$. For a given central Nb^{5+} ion the probability that it has a nBn configuration (N_{Mg},N_{Sc},N_{Nb}) is

$$P_{CR}(N_{Mg},N_{Sc},x)=\frac{6!}{N_{Mg}!N_{Sc}!N_{Nb}!}(C_{Mg})^{N_{Mg}}$$
$$\times(C_{Sc})^{N_{Sc}}(C_{Nb})^{N_{Nb}}. \quad (3)$$

In our assignments the narrow lines are configurations with no Nb^{5+} nearest B neighbors. The probabilities are thus

$$P_{CR}(N_{Mg},6-N_{Mg},x)$$
$$=\frac{6!}{N_{Mg}!(6-N_{Mg})!}\left(\frac{1-x}{3}\right)^{N_{Mg}}\left(\frac{x}{2}\right)^{6-N_{Mg}}. \quad (4)$$

This formula gives negligible values ($<1.6\%$) for all narrow lines at all PSN concentrations. Since typical NMR intensities for the narrow lines are on the order of 10% (Table I), this model fails to account for the observed NMR intensities and is an inappropriate description of B-site ordering. Moreover, it is important to appreciate that even in the disordered samples the NMR MAS spectral intensities cannot be described by the CR model (Table I). This implies that there is significant short-range order even in the as sintered materials.

B. Random site

This model assumes that along the [111] direction the layers of B cations alternate between pure Nb^{5+} and a random mixture of Mg^{2+}, Sc^{2+} and the remaining Nb^{5+} (Fig. 5). The alternation occurs along all four body diagonals. The name "random site"[16] is used instead of the previous "random layer"[15] since the word "layer" might suggest that the 1:1 ordering is only in one direction. The stoichiometric formula is $Pb(\beta'_{1/2}\beta''_{1/2})O_3$, with $\beta'=$ random mixture $[Mg_{2(1-x)/3}Sc_xNb_{(1-x)/3}]$ and $\beta''=Nb$. Half of the B cations are on β' sites, and half are on β'' sites, i.e., $p_{\beta'}=1/2, p_{\beta''}=1/2$. Within the mixed layer, the concentrations are $C_{\beta'Mg}=2(1-x)/3, C_{\beta'Sc}=x, C_{\beta'Nb}=(1-x)/3$. The total Nb^{5+} concentration $C_{Nb}=(4-x)/6$ is restored by calculating $p_{\beta'}C_{\beta'Nb}+p_{\beta''}$.

Each Nb^{5+} cation in the mixture layer (β') has six Nb^{5+} nearest B-site neighbors in the two adjacent pure Nb^{5+} layers (β''). Therefore the probability of having a B-cation which is β'-type Nb^{5+} with nBn configuration (N_{Mg},N_{Sc},N_{Nb}) is

$$P_{\beta'Nb}(N_{Mg},N_{Sc},x)=p_{\beta'}C_{\beta'Nb}\delta(N_{Mg},N_{Sc}), \quad (5)$$

where $\delta=1$ for $N_{Mg}=0$ and $N_{Sc}=0$, 0 otherwise. Each Nb^{5+} cation in the pure layer (β'') has 28 possible configurations of nearest B neighbors from the two adjacent mixture layers (β'). The probability of having a B cation which is β''-type Nb^{5+} with nBn configuration (N_{Mg},N_{Sc},N_{Nb}) is

$$P_{\beta''Nb}(N_{Mg},N_{Sc},x)=p_{\beta''}\frac{6!}{N_{Mg}!N_{Sc}!N_{Nb}!}(C_{\beta'Mg})^{N_{Mg}}$$
$$\times(C_{\beta'Sc})^{N_{Sc}}(C_{\beta'Nb})^{N_{Nb}}. \quad (6)$$

The probability of having a B-cation which is Nb^{5+} with nBn configuration (N_{Mg},N_{Sc},N_{Nb}) is the simply sum of Eqs. (5) and (6),

$$P_{Nb}(N_{Mg},N_{Sc},x)=P_{\beta'Nb}(N_{Mg},N_{Sc},x)$$
$$+P_{\beta''Nb}(N_{Mg},N_{Sc},x). \quad (7)$$

The summation of the probability over N_{Mg} and N_{Sc} is, not surprisingly, $C_{Nb}=(4-x)/6$. Thus normalization of Eq. (7) gives the probability of having a Nb^{5+} cation with nBn configuration (N_{Mg},N_{Sc},N_{Nb}),

$$P_{RS}(N_{Mg},N_{Sc},x)=\frac{6}{4-x}P_{Nb}(N_{Mg},N_{Sc},x). \quad (8)$$

For the narrow lines where $N_{Nb}=0$, the RS prediction is found to be related to the completely random prediction [Eq. (4)] by

$$P_{RS}(N_{Mg},6-N_{Mg},x)=\frac{192}{4-x}P_{CR}(N_{Mg},6-N_{Mg},x). \quad (9)$$

Therefore, for MAS spectral components assigned to $(N_{Mg},6-N_{Mg},0)$ configurations, it is obvious that the RS model yields much larger intensities than the CR model (48 times at $x=0$, and 64 times at $x=1$).

TABLE II. Random site prediction and experimental results of PMN and five ordered PMN-PSN solid solutions at 19.6 T. Contributions of 28 configurations are arranged according to $(N_{Mg}N_{Sc}N_{Nb})$ (see Fig. 6). The predicted line intensities (for the seven narrow lines and two broad distributions) are compared with experimental intensities which are in parentheses.

x=0.0

```
                      6Nb
                      25.1
                   1.2   0.0
                6.2   0.0   0.0            D1: 49.0
 D2: 44.4    16.5  0.0   0.0   0.0            (39.9)
 (45.3)    24.7  0.0   0.0   0.0   0.0
         19.8  0.0   0.0   0.0   0.0   0.0
 6Mg  6.6  0.0  0.0   0.0  0.0   0.0   0.0  6Sc
      6.6  0.0  0.0   0.0  0.0   0.0   0.0
    (14.8  0.0  0.0   0.0  0.0   0.0   0.0)
```

x=0.6

```
                      6Nb
                      11.8
                   0.0   0.0
                0.0   0.1   0.2            D1: 28.0
 D2: 1.3     0.1  0.5   1.2   0.9            (16.0)
 (0)       0.1  1.1   3.6   5.4   3.1
         0.1  1.1   4.8   10.8  12.2  5.5
 6Mg  0.0  0.4  2.4   7.2  12.2  11.0  4.1  6Sc
      0.0  0.4  2.4   12.1 23.0  23.2  9.6
    (1.2  2.7  6.8   18.2 24.8  21.7  8.4)
```

x=0.1

```
                      6Nb
                      23.1
                   0.7   0.1
                3.4   1.1   0.1            D1: 57.7
 D2: 33.2    9.0  4.5   0.8   0.0            (44.8)
 (32.6)    13.5  9.0   2.2   0.3   0.0
         10.8  9.0   3.0   0.5   0.0   0.0
 6Mg  3.6  3.6  1.5   0.3  0.0   0.0   0.0  6Sc
      3.6  3.6  1.5   0.3  0.0   0.0   0.0
    (11.7  8.5  2.4   0.0  0.0   0.0   0.0)
```

x=0.7

```
                      6Nb
                      9.1
                   0.0   0.0
                0.0   0.0   0.1            D1: 19.4
 D2: 0.4     0.0  0.2   0.5   0.6            (13.1)
 (0)       0.0  0.3   1.6   3.7   3.3
         0.0  0.3   2.1   7.5   13.1  9.2
 6Mg  0.0  0.1  1.1   5.0  13.1  8.3  10.7  6Sc
      0.0  0.1  1.1   7.1  20.6  31.4  19.9
    (0.3  0.7  2.9   10.9 23.6  31.5  16.9)
```

x=0.2

```
                      6Nb
                      21.1
                   0.3   0.1
                1.7   1.3   0.2            D1: 65.2
 D2: 22.5    4.5  5.1   1.9   0.2            (45.4)
 (28.6)    6.8  10.2  5.8   1.4   0.1
         5.5  10.2  7.7   2.9   0.5   0.0
 6Mg  1.8  4.1  3.8   1.9  0.5   0.1   0.0  6Sc
      1.8  4.1  3.8   1.9  0.5   0.1   0.0
    (7.7  11.3  7.0   0.0  0.0   0.0   0.0)
```

x=0.9

```
                      6Nb
                      3.2
                   0.0   0.0
                0.0   0.0   0.0            D1: 20.7
 D2: 0       0.0  0.0   0.0   0.1            (17.2)
 (0)       0.0  0.0   0.0   0.3   1.1
         0.0  0.0   0.1   0.6   4.2   11.4
 6Mg  0.0  0.0  0.0   0.4  4.2   22.9  51.4  6Sc
      0.0  0.0  0.0   0.4  4.2   22.9  51.4
    (0.0  0.0  0.0   0.0  5.0   25.4  52.5)
```

The random site model is in very good qualitative agreement with the experimental MAS line intensities (Table II). The RS probabilities of the 28 configurations can be used to predict the integrated MAS intensities for all concentration x. In Table II, the 28 probabilities for each concentration are arranged on triangular grid, as in Fig. 6. Theoretical intensities of the seven narrow lines and two broad lines are derived and compared with the experimental intensities (in parentheses) obtained by deconvolution of the MAS spectra obtained at 19.6 T.

Although the NMR results strongly support the RS model, we would prefer to achieve quantitative agreement. Closer inspection of the overall line shapes reveals that RS predicts intensities too low for the narrow lines with relatively large numbers of Mg^{2+} cations (≥ 3) in the nBn configuration. For quantitative comparison, we predict the MAS line shapes by using RS populations (from Table II) and compare them with experimental spectra (Fig. 8). For high concentrations $x=0.7$ and 0.9, the agreement is very good. However, for the lower scandium concentrations, peak intensities corresponding to configurations (6,0,0), (5,1,0), (4,2,0), and (3,3,0) are consistently underestimated. As illustrated in Fig. 8, such deficiencies cause a dramatic mismatch in the appearance of the spectra. This is particularly demonstrated in the sharp peak of the PMN associated with six Mg^{2+} neighbors, Nb(6,0,0). These comparisons attest the high specificity of NMR and its unique ability to probe local order and disorder in solids.

C. Modified RS model

We believe that the primary limitation of the RS model lies in its assumption that within the mixed layers all three
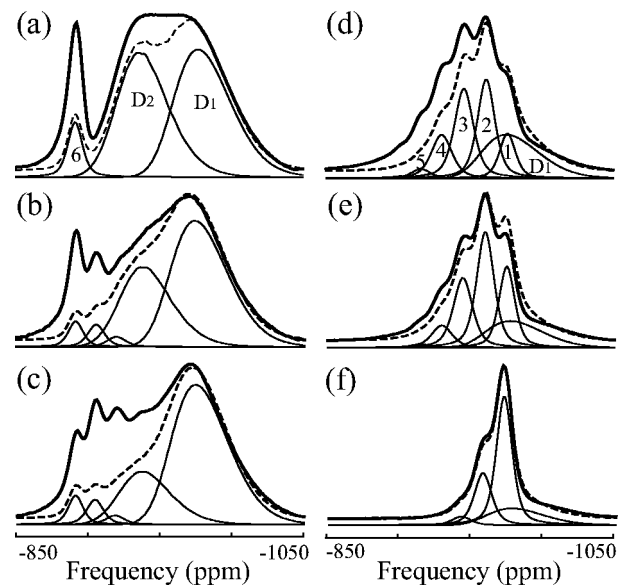

FIG. 8. Random site predictions of line components (thin solid) and total intensities (dotted line), compared with MAS spectra (solid bold) at 19.6 T for $(1-x)$PMN-xPSN samples. (a) PMN; (b)–(f) ordered samples with PSN concentration $x=0.1$, 0.2, 0.6, 0.7, and 0.9, respectively.

types of cations (Mg^{2+}, Sc^{3+}, and Nb^{5+}) are distributed completely randomly. In fact their differences in valence charge, ionic size, and electronegativity are all possible driving forces for cation preference within the mixture layers. Pragmatically, it appears that there is some degree of Mg^{2+} clustering on the mixture layers, so as to enhance the intensities for the niobiums with relatively large number of Mg^{2+} in the nearest B neighbor configuration.

This hypothesis can be most simply examined by Monte Carlo simulation on PMN, because the deviation of RS model is most serious at this concentration ($x=0$), it is simplest to simulate, and there is only one unlike-pair energy to consider (between Mg^{2+} and Nb^{5+}). The B-site lattice is initialized according to the random site model, that is, [111] planes alternate between pure Nb^{5+} (β'') and random mixture of the Mg^{2+} and the remaining Nb^{5+} (β'). The lattice size ($30\times30\times30$) is large enough to ensure that the 28 nBn probabilities predicted by the RS model are reproduced by counting the nearest B configurations on the lattice. The $[111]_{1:1}$ ordering, which is the compromise between the long-range electrostatic interactions among B cations and the local effect of large Pb^{2+} covalency,[10–14] should be maintained throughout the simulation. For this purpose, the pure B sublattice (β'') is fixed and the Monte Carlo algorithm is only applied on the mixed B sublattice (β'). Since swapping two cations of the same type does not change energy, we may set like-pair energies to zero and only consider the unlike-pair energy between Mg^{2+} and Nb^{5+}. Thus the Monte Carlo algorithm is: randomly pick a nearest-neighbor pair on the mixture sublattice and then attempt to swap them. If the total energy decreases, accept the swap; otherwise, accept with probability $\exp(-\Delta E/RT)$, where ΔE is the energy difference resulting from the swap, R is the universal gas constant, and T is temperature. Repeat the process for a large number of times (8.1×10^8) and then evaluate the 28 nBn probabilities over the whole B lattice. The experimental intensity (14%) of the all-magnesium (6,0,0) narrow line is reproduced when the unlike-pair energy is adjusted to $-1.3RT$. At room temperature (300 K) this energy is -3.25 kJ/mole, which is interestingly close to -3.14 kJ/mole, the enthalpy change associated with the RS order-disorder transition.[16] Whatever their origin, whether differences in charge, size, or electronegativity, these driving forces bring the B lattice to the $[111]_{1:1}$ ordering. They also result in the mixture layers exhibiting some degree of clustering, rather than complete randomness.

The Monte Carlo simulation produces intensities for the two distributions, 50.0% for D_1 and 35.2% for D_2. These agree very well with experimental values 48.4% and 38.6% at 14 T. At 19.6 T, the values are 39.9% and 45.3% for D_1 and D_2, respectively. The inconsistency between the two fields results from the uncertainties in the partition of the overlapping D_1 and D_2 Gaussian distributions in PMN MAS spectra. In the Appendix it is shown that, at both fields, consistent D_1 and D_2 intensities for the PMN broad peak can be achieved by using the Czjzek distribution function of ν_Q and η.[32–34] The Czjzek scheme, however, does not affect any intensities of the narrow components ($N_{Nb}=0$) significantly.
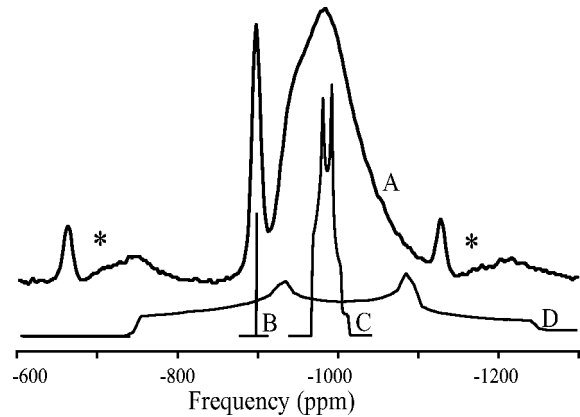

FIG. 9. Experimental PMN MAS spectrum with quadrupolar line shapes simulated according to parameters given by Shore and co-workers (Refs. 20 and 21). (A) [93]Nb PMN MAS spectrum collected at 14 T, sample spinning speed 34 kHz; sidebands are marked by stars. (B) Simulated line with $C_Q=1.2$ MHz, $\eta=0.5$, $\delta_{iso}^{CS}=-896$ ppm. (C) Simulated line shape with $C_Q=17$ MHz, $\eta=0.5$, $\delta_{iso}^{CS}=-960$ ppm. The isotropic second quadrupolar shift $\delta_{iso}^{2Q}=-20$ ppm, the bary center ($\delta_{iso}^{CS}+\delta_{iso}^{2Q}$) of this line is at -980 ppm. (D) Simulated line shape with $C_Q=62$ MHz, $\eta=0.5$, $\delta_{iso}^{CS}=-709$ ppm. $\delta_{iso}^{2Q}=-271$ ppm, and the bary center is also at -980 ppm.

It represents another way of partitioning the broad components arising from $N_{Nb}\neq0$. Moreover, for concentrations other than $x=0$, the Gaussian functions give consistent intensities at both magnetic fields for the two broad components. Because of overall consistency and more intuitive interpretation, we report quantitative results from fits using Gaussian distribution functions.

VI. DISCUSSION

A. PMN

Assignment of the MAS spectra of PMN remains controversial: the number of nonequivalent sites and their associated NMR parameters differ considerably in the literature. For instance, Cruz *et al.* analyzed a 3QMAS experiment (at 9.4 T) to obtain $C_Q=8.5$ MHz, $\eta=0.5$ ($P_Q=8.8$ MHz) for the sharp peak, which is comparable to our estimated value $P_Q = 13$ MHz. They simply assign the broad peak to a single site with $C_Q=21.5$ MHz, $\eta=0.8$ ($P_Q=23.7$ MHz).[19] Using nutation NMR (at 9.4 T) Prasad *et al.*, claimed to observe three sites, with estimated C_Q <1.2, ~17, and >62 MHz.[20] In their 14-T MAS study, they associated the $C_Q<1.2$-MHz nutation site with the sharp MAS peak, and both $C_Q\sim17$- and $C_Q>62$-MHz sites with the broad peak near -980 ppm.[21] However, these assignments are inconsistent with our results. First, our direct analyses of MAS spectra show $C_Q>12$ MHz for the sharp peak. Second, the broad peak cannot have $C_Q>62$ MHz for the following reasons. The line shapes simulated with parameters from Refs. 20 and 21 are compared with our experimental MAS spectrum of PMN at 14 T (Fig. 9). The line with small $C_Q=1.2$ MHz has negligible second-order quadrupolar linewidth; it is far too narrow to match the narrow
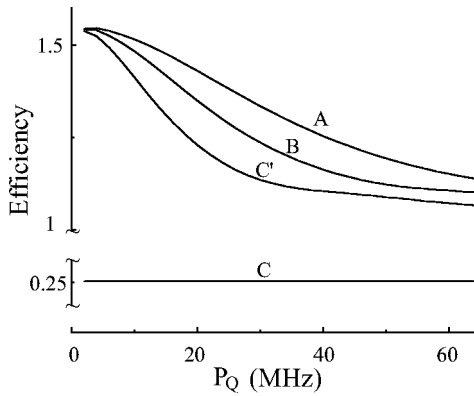
FIG. 10. Pulse sequence efficiency as a function of quadrupole product (P_Q). Results are obtained from numerical simulation assuming infinite sample spinning speed. Vertical axis is in arbitrary units. (A) Pulse conditions used in MAS experiments at 19.6 T; $\nu_1 = 71$ kHz, $t_p = 0.7$ μs. (B) Conditions used in MAS experiments at 14 T; $\nu_1 = 50$ kHz, $t_p = 1$ μs. (C) Conditions used by Fitzgerald *et al.* in MAS experiments at 14 T; $\nu_1 = 32.5$ kHz, $t_p = 0.25$ μs (Ref. 21). (C′) Same as (C) except for $t_p = 1.54$ μs. A, B, and C′ have flip angle of 18°; C has flip angle of 2.9°.

peak of the experimental spectra. On the other hand, the enormously large $C_Q = 62$ MHz yields a line shape much wider than the broad experimental MAS peak. Moreover, the large second-order isotropic shift $\delta_{\text{iso}}^{2Q} = -271$ ppm has to be compensated for by setting $\delta_{\text{iso}}^{\text{CS}} = -709$ ppm in order to keep the bary center ($\langle \delta_{1/2} \rangle = \delta_{\text{iso}}^{\text{CS}} + \delta_{\text{iso}}^{2Q}$) near -980 ppm. However, such a $\delta_{\text{iso}}^{\text{CS}}$ value does not fit with the -1113–-951-ppm range observed in studies on eight crystalline alkali and lead niobates.[31]

Regardless of these inconsistencies, it is certain that the sharp peak has a C_Q much larger than 1.2 MHz. Any site with $C_Q < 1.2$ MHz would be easily observed in MAS spectra; the RF excitation is efficient, and the intensity is strongly enhanced by such narrow linewidth. It should also be clear that the broad peak consists of at least two contributions, but both have $C_Q \ll 62$ MHz.

To further confirm these conclusions we simulated the efficiency of various MAS pulse sequences used here and in the literature, the results are shown in Fig. 10. The efficiency is averaged over all orientations, thus it is proportional to the integrated spectral intensity. In our experiments (curves A and B) the single pulse has a flip angle of 18°. These efficiencies decay monotonically with increasing P_Q (e.g., for curve A, the efficiency is 1.54 for $P_Q = 1.2$ MHz, 1.49 for $P_Q = 13$ MHz, 1.33 for $P_Q = 30$ MHz, and 1.10 for $P_Q = 62$ MHz). Uniform but very low efficiency (0.25) was obtained by using the sequence used by Fitzgerald *et al.* with a small flip angle of 2.9° (curve C).[21] If there is a site with large $P_Q > 62$ MHz, it should be easier to detect under the conditions of our MAS experiments. However, we did not observe such a site. Compared with the MAS spectrum of Fitzgerald *et al.*,[21] the sharp peak in our PMN spectrum has lower intensity. This contradicts the higher sensitivity to small P_Q in our experiments. It is likely that the intensity differences in the sharp peak and (potential) disagreement regarding the existence of a large C_Q site ($P_Q > 62$ MHz) are
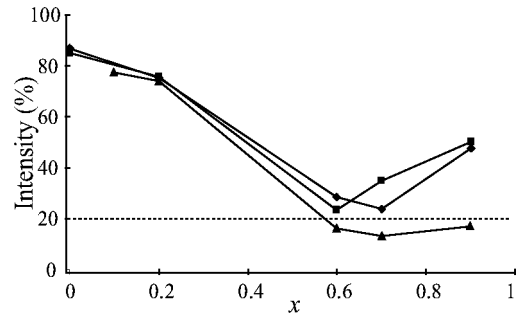

FIG. 11. The combined intensity of D_1 and D_2 as a function of PSN concentration x. Disordered samples at 14 T (diamond), disordered samples at 19.6 T (square), ordered samples at 19.6 T (triangle).

the results of different samples used in the two studies. The properties of these ceramics are known to be highly dependent on preparation and ordering procedures.

In passing, the calculations illustrated in Fig. 10 show that under our experimental conditions, the excitation efficiency is relatively even for both sharp peaks ($P_Q \sim 13$ MHz) and broad peaks ($P_Q \sim 30$ MHz). Thus for all our PMN-PSN MAS spectra, corrections to intensities listed in Table I are small ($< 2\%$) and have been omitted.

According to our MAS results, the observed C_Q values in PMN are all between 12 and 35 MHz. A perfect perovskite crystal would have cubic symmetry, and thus zero EFG. The relatively large C_Q values are not surprising, since significant lattice distortions (positional disorder) have been reported in PMN.[35]

B. PMN-PSN

For the PMN-PSN MAS spectra and their deconvolution results, several observations can be made as follows. First, at any given concentration and field (see Fig. 4), the spectra of disordered and ordered samples are qualitatively similar. The samples are disordered in the sense that their XRD patterns lack the (1/2,1/2,1/2) supercell reflection associated with 1:1 chemical order in the [111] direction.[16] However, it is important to appreciate that XRD detects long or intermediate-range order, while NMR probes local environments. In the disordered samples the ordered domains are on the nanoscale (2–5 nm) making them difficult to detect by XRD. The similarity in NMR spectra leads to the conclusion that *locally*, the *B*-site (chemical) ordering in the disordered and ordered samples are very similar.

Second, the combined intensity of the distributions D_1 and D_2 is plotted against PSN concentration x in Fig. 11. For low x, the intensities for ordered and disordered samples are fairly similar; difference between them becomes apparent only after $x > 0.6$. Frequency-dependent dielectric measurements reveal that for $x \leq 0.5$ relaxor behavior is observed in both ordered and disordered materials; for $x \geq 0.6$, relaxor behavior is observed in disordered materials, but normal ferroelectric behavior is seen in ordered materials.[16] Thus there appears to be a correlation between the integrated intensity of the distributions and the dielectric response. The

combined intensity may be used as an indicator of whether the sample is a relaxor or normal ferroelectric. Empirically it appears that when the distribution intensity is above 20%, the material behaves as a relaxor, while below this, as a normal ferroelectric, regardless of the domain size determined by TEM or the degree of order characterized by XRD.[16]

Third, the position of each narrow line shifts slightly to higher frequency as the PSN concentration x increases. The components with intensity below 1% do not have reliable position parameters, thus they are neglected in the following analysis. For ordered samples at 19.6 T (Table I), linear fitting shows that the shifts are 1.3, 1.3, 1.1, 0.7, 0.7, 0.7, and 0.6 ppm with x increment of 0.1, for narrow lines 0–6, respectively. We attribute these shifts to the slight increase in the lattice constant resulting from adding PSN; the average B-cation radius 0.69 Å $[(R_{Sc}+R_{Nb})/2, R_{Sc}=0.745, R_{Nb}=0.64]$, which is larger than the 0.67 Å for PMN $[(R_{Mg}+2R_{Nb})/3, R_{Mg}=0.72]$. de Dios et $al.$ reported positive shift derivative with respect to bond extension ranging from 4 to 2784 ppm/Å in most cases.[36] It is further supported by the pattern that the shift increases with the number of Sc in nBn. The unit cells expand most around the 93Nb having six Sc nBn (line 0), and the least around those having zero Sc nBn (line 6). For disordered samples, the shifts are 1.3, 1.2, 1.1, 1.1, 0.64, 0.47, and 0.68 ppm at 19.6 T; and 1.5, 1.3, 1.2, 0.5, 0.6, 0.6, and −0.4 ppm at 14 T.

Fourth, for the ordered samples, the linewidths of the seven narrow lines ($N_{Nb}=0$) do not change noticeably with x. In the simulation, they are set constant for each narrow line. Specifically, they are 13, 14.3, 15.7, 17.0, 15.3, 13.7, and 12 ppm for lines 0–6 respectively. These values correlate interestingly with the "purity" of the nBn configuration, that is, the $N_{Sc}=6$ (line 0) and $N_{Mg}=6$ (line 6) lines are narrowest, and the $N_{Mg}=N_{Sc}=3$ (line 3) is widest. This is because the five ($N_{Mg}=1,2,\cdots 5$) "mixed" configurations have lower symmetry than the two "pure" configurations. Moreover, each of the three "mixed" configurations with $N_{Mg}=2$, 3, and 4 have two different spatial arrangements among the six nBn sites. For $N_{Mg}=2$, the two Mg^{2+} ions can occupy both ends of one of the three orthogonal axes, or each of them occupy one end of two different axes; for $N_{Mg}=3$, each of them may occupy one end of the three axes, or two Mg^{2+} ions are on one axis, while the other Mg^{2+} is on a different axis; and the $N_{Mg}=4$ case has $N_{Sc}=2$, which is similar to the $N_{Mg}=2$ case. The different spatial arrangements result in slightly different NMR parameters, which result in broadening of the line shape.

Finally, in disordered samples there is concentration dependence of the linewidth for narrow lines. Moreover, the linewidths for the disordered samples are typically 0.3–3 ppm wider than those for the ordered samples. The wider linewidths reveal that the disordered samples have more distorted local environments and/or a wider range of spatially different but topologically identical environments.

VII. CONCLUSIONS

93Nb MAS NMR experiments have been performed on perovskite relaxor ferroelectric PMN-PSN solid solutions at high magnetic fields and fast sample spinning speeds. The resolution of the experiments is sufficient to allow assignments of MAS spectral components to 93Nb sites in 28 nearest B neighbor configurations. Seven narrow peaks and two broad components have been identified. The seven narrow peaks have been assigned to the seven configurations devoid of Nb^{5+}; and are labeled 0–6 according to the number of Mg^{2+} in the configurations. The two broad components D_1 and D_2 have been respectively assigned to 18 and 3 configurations containing Nb^{5+}. These spectral assignments facilitate quantitative evaluation of, and differentiation between, different models of B-site (chemical) disorder. The completely random model was ruled out and the random site model is shown to be in qualitative agreement with the NMR experiments. However, at compositions with low PSN concentration, the RS model underestimates intensities for the narrow spectral components corresponding to nearest B neighbor configurations with large Mg^{2+} number ($N_{Mg}>3$). This remaining small discrepancy from predictions of the RS model is most probably the result of its assumption of complete compositional randomness within the mixed layers. To explain this observation and obtain quantitative agreement with observed NMR intensities, we propose an enthalpic contribution which promotes clustering of Mg^{2+} cations on the mixed B sublattice. Monte Carlo simulations on PMN confirm that when the unlike-pair energy between Nb^{5+} and Mg^{2+} is −3.2 kJ/mole, quantitative agreement of intensities are achieved.

The seven narrow peaks have small quadrupole coupling constants ($C_Q \sim 12$ MHz) presumably because the Mg^{2+} and Sc^{3+} are similar in terms of charge, size, and electronegativity. These peaks are separated by around 14 ppm. Empirically it appears that the isotropic chemical shift decreases by about 14 ppm when each Mg^{2+} is replaced by Sc^{3+} in the nearest B neighbor configuration. The broad components have distributions of both chemical shifts and quadrupole coupling constants. For D_1, the mean $\mu(\delta_{iso}^{CS})$ ranges from −953 to −951 ppm, standard deviation $\sigma(\delta_{iso}^{CS}) = 10.9$ ppm, $\mu(C_Q)=28.6$ MHz, and $\sigma(C_Q)=3.9$ MHz; for D_2, the mean $\mu(\delta_{iso}^{CS})$ varies from −922 to −919.5 ppm, standard deviation $\sigma(\delta_{iso}^{CS})=12.9$ ppm, $\mu(C_Q)=24.4$ MHz, and $\sigma(C_Q)=5.1$ MHz. The large quadrupole coupling constants, which are about double the C_Q for narrow peaks, result from distortion due to the mismatch of charge, size, and electronegativity of Nb^{5+} containing nBn configurations. A doubled C_Q means a four fold increasing in linewidth due second-order quadrupole broadening. Therefore the line shapes corresponding to these Nb^{5+} containing configurations severely overlap and result in broad components. Two-dimensional 93Nb 3QMAS spectra have been collected and are currently being analyzed. 3QMAS spectra provide site-specific chemical shift and quadrupolar parameters. To date these results are consistent with MAS results described in the paper.

Spectra of ordered and disordered samples are qualitatively similar. This indicates that $locally$ the B-site (chemical) ordering in ordered (heat treated) and disordered (as sintered) samples are similar. The combined intensity of

distributions D_1 and D_2 correlates with dielectric response. Empirically, the material is a relaxor ferroelectric if the intensity is above 20%, and a normal ferroelectric if the intensity is below this, regardless of the domain size or degree of order.

To provide comprehensive studies on these complex systems, [45]Sc MAS and 3QMAS spectra, and variable temperature [207]Pb MAS and 2D-PASS (Ref. 37) spectra are also being analyzed. In conclusion, multinuclei NMR studies, as have been demonstrated by the [93]Nb MAS results, can provide a wealth of detailed information on cation order and dynamics in complex relaxor ferroelectric solid solutions.

APPENDIX: CZJZEK DISTRIBUTION SCHEME FOR QUADRUPOLAR PARAMETERS

The analysis described in the result section (Sec. III) uses Gaussian distributions of NMR spectral parameters to fit the MAS line shapes. For D_1 and D_2, we used the simple Gaussian distribution of parameters $\delta_{\mathrm{iso}}^{\mathrm{CS}}$ and ν_Q, and chose unique η values (0.4 for D_1 and 0 for D_2) by optimizing line fitting for spectra at all x at both 14 and 19.6 T. Another choice is the Czjzek function, which has been successfully used to describe distributions of quadrupole parameters in amorphous fluorides by Czjzek *et al.* and Bureau *et al.*[32–34] This function allows for simultaneous variations of η as well as ν_Q,

$$P(\nu_Q, \eta) = \frac{1}{\sqrt{2\pi}\sigma^d} \nu_Q^{d-1} \eta \left(1 - \frac{\eta^2}{9}\right) \exp\left[-\frac{\nu_Q^2(1 + \eta^2/3)}{2\sigma^2}\right],$$

$$\text{(A1)}$$

where σ controls both width and most probable value of ν_Q distribution at a given η, and d is related to the number of independent random components of the EFG tensor ($d \leqslant 5$). A decreased value of d reflects local geometrical constraints.

For PMN spectra at both 14 and 19.6 T, $d = 3$, 4, and 5 are all able to fit the spectra, but only $d = 4$ gives consistent D_1 and D_2 intensities. We thus pick $d = 4$ and use this to deconvolute all MAS spectra (see Fig. 12). The fit quality is comparable to the Gaussian scheme reported in the text. The parameters (position and FWHM) of narrow components are the same as in the Gaussian scheme (Table I), and their intensities change only slightly. D_1 has a Czjzek distribution of quadrupolar parameters ($\sigma = 450$ kHz, $d = 4$) and a Gaussian distribution of isotropic chemical shift [mean $\mu(\delta_{\mathrm{iso}}^{\mathrm{CS}})$ ranges
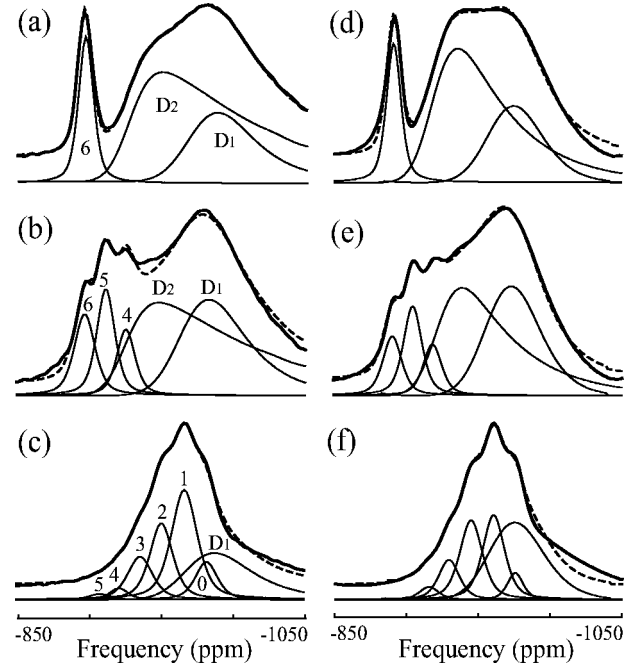

FIG. 12. Deconvolution with Czjzek distribution of quadrupolar parameters. MAS spectra, which are represented by bold solid lines, are collected at 14 T (left column) and 19.6 T (right column) for disordered samples with concentrations $x = 0$, 0.2, and 0.7 (from top to bottom). Thin solid lines are deconvoluted lines, of which $0-6$ are simple Gaussian/Lorentzian, and D_1 and D_2 consist Czjzek distribution of quadrupolar parameters and Gaussian distribution of isotropic chemical shift. Dashed lines are sum of thin solid lines.

between -970 and -965 ppm at 14 T, or from -963 to -960 at 19.6 T, standard deviation $\sigma(\delta_{\mathrm{iso}}^{\mathrm{CS}}) = 15.9$ ppm]. D_2 has a Czjzek distribution of quadrupolar parameters ($\sigma = 750$ kHz, $d = 4$) and a Gaussian distribution of isotropic chemical shift [mean $\mu(\delta_{\mathrm{iso}}^{\mathrm{CS}})$ ranges from -923 to -922 ppm at 14 T, or from -920 to -915 at 19.6 T, standard deviation $\sigma(\delta_{\mathrm{iso}}^{\mathrm{CS}}) = 11.6$ ppm]. The integrated intensities of the distributions D_1 and D_2 obtained from the Czjzek deconvolution are listed in Table III.

The Czjzek functions give consistent integrated intensities for D_1 and D_2 at both fields. However, except for PMN, the

TABLE III. Integrated intensities (%) of broad peak distribution components with Czjzek deconvolution scheme.

x		0	0.1	0.2	0.6	0.7	0.9
Disorder	D_1	24.2			29.2	34.0	28.9	63.4
14 T	D_2	62.8			46.2			
Disorder	D_1	25.4			32.7	27.9	41.0	58.6
19.6 T	D_2	60.3			43.6			
Ordered	D_1		35.6	37.4	16.9	15.1	19.3
19.6 T	D_2		43.5	39.0			

consistency is similar to that using Gaussian distribution functions (cf. Table I). The Gaussian function offers straightforward interpretation of the mean and standard deviation of the distribution of NMR parameters. Moreover, the Czjzek distribution was derived on the basis of an ionic model,[32,33] while in our PMN-PSN system bond covalency may play an important role. For these reasons, we chose to adopt Gaussian distribution functions in the text.

*Author to whom correspondence should be addressed. Electronic address: gina@physics.wm.edu

[1] L. E. Cross, Ferroelectrics **151**, 305 (1994).

[2] R. E. Newnham, NIST Spec. Publ. **804**, 39 (1996).

[3] K. Uchino, *Piezoelectric Actuators and Ultrasonic Motors* (Kluwer Academic Publishers, Boston, 1996).

[4] S.-E. Park and T. R. Shrout, J. Appl. Phys. **82**, 1804 (1997).

[5] H. B. Krause, J. M. Cowley, and J. Whealey, Acta Crystallogr., Sect. A: Cryst. Phys., Diffr., Theor. Gen. Crystallogr. **35**, 1015 (1979).

[6] E. Husson, M. Chubb, and A. Morell, Mater. Res. Bull. **23**, 357 (1988).

[7] J. Chen, H. M. Chan, and M. P. Harmer, J. Am. Ceram. Soc. **72**, 593 (1989).

[8] G. A. Smolenskii, I. G. Siny, R. V. Pisarev, and E. G. Kuzminov, Ferroelectrics **12**, 135 (1976).

[9] E. Husson, L. Abello, and A. Morell, Mater. Res. Bull. **25**, 539 (1990).

[10] B. P. Burton and E. Cockayne, Phys. Rev. B **60**, R12 542 (1999).

[11] B. P. Burton, Phys. Rev. B **59**, 6087 (1999).

[12] B. P. Burton, J. Phys. Chem. Solids **61**, 326 (2000).

[13] H. Gui, X. Zhang, and B. Gu, J. Phys.: Condens. Matter **8**, 1491 (1996).

[14] Z. Wu and H. Krakauer, Phys. Rev. B **63**, 184113 (2001).

[15] M. A. Akbas and P. K. Davies, J. Am. Ceram. Soc. **80**, 2933 (1997).

[16] P. K. Davies, L. Farber, M. Valant, and M. A. Akbas, in *Fundamental Physics of Ferroelectrics 2000*, edited by R. E. Cohen, AIP Conf. Proc. No. 535 (AIP, Melville, NY, 2000), p. 38.

[17] P. K. Davies and M. A. Akbas, J. Phys. Chem. Solids **61**, 159 (2000).

[18] M. D. Glinchuk, V. V. Laguta, I. P. Bykow, S. Nokhrin, V. P. Bovtun, M. A. Leschenko, J. Rosa, and L. Jastrabik, J. Appl. Phys. **81**, 3561 (1997).

[19] L. P. Cruz, J. Rocha, J. D. P. de Jesus, J. M. Savariault, and J. Galy, Solid State Nucl. Magn. Reson. **15**, 153 (1999).

[20] S. Prasad, P. Zhao, J. Huang, and J. S. Shore, Solid State Nucl. Magn. Reson. **14**, 231 (1999).

[21] J. J. Fitzgerald, S. Prasad, J. Huang, and J. S. Shore, J. Am. Ceram. Soc. **122**, 2556 (2000).

[22] A. Llor and J. Virlet, Chem. Phys. Lett. **152**, 248 (1988).

[23] F. Delaglio, G. W. Vuister, G. Zhu, and J. Pfeifer, J. Biomol. NMR **6**, 277 (1995).

[24] D. Massiot, F. Franck, M. Capron, I. King, S. L. Calve, B. Alonso, J.-O. Durand, B. Bujoli, Z. Gan, and G. Hoatson, Magn. Reson. Chem. **40**, 70 (2002).

[25] A. Samoson, E. Kundla, and E. Lippmaa, J. Magn. Reson. (1969-1992) **49**, 350 (1982).

[26] M. H. Cohen and F. Reif, *Solid State Physics: Advances in Research and Applications* (Academic Press, New York, 1957), Vol. 5, pp. 321–438.

[27] R. D. Shannon, Acta Crystallogr., Sect. A: Cryst. Phys., Diffr., Theor. Gen. Crystallogr. **A32**, 751 (1976).

[28] A. M. James and M. P. Lord, *Macmillan's Chemical and Physical Data* (Macmillan, London, 1992).

[29] I.-W. Chen, P. Li, and Y. Wang, J. Phys. Chem. Solids **57**, 1525 (1996).

[30] W. Dmowski, M. K. Akbas, P. K. Davies, and T. Egami, J. Phys. Chem. Solids **61**, 229 (2000).

[31] S. Prasad, P. Zhao, J. Huang, J. J. Fitzgerald, and J. S. Shore, Solid State Nucl. Magn. Reson. **19**, 45 (2001).

[32] G. Czjzek, J. Fink, F. Gotz, and H. Schmidt, Phys. Rev. B **23**, 2513 (1981).

[33] G. Czjzek, Phys. Rev. B **25**, 4908 (1982).

[34] B. Bureau, G. Silly, J. Buzare, C. Legein, and D. Massiot, Solid State Nucl. Magn. Reson. **14**, 181 (1999).

[35] H. D. Rosenfeld and T. Egami, Ferroelectrics **158**, 351 (1994).

[36] A. C. de Dios, A. Walling, I. Cameron, C. I. Ratcliffe, and J. A. Ripmeester, J. Phys. Chem. A **104**, 908 (2000).

[37] F. Fayon, C. Bessada, A. Douy, and D. Massiot, J. Magn. Reson., Ser. A **137**, 116 (1999).